

Airborne Particle Communication Through Time-varying Diffusion-Advection Channels

Fatih Merdan, Ozgur B. Akan, Fellow, IEEE

Abstract—Particle-based communication using diffusion and advection has emerged as an alternative signaling paradigm recently. While most existing studies assume constant flow conditions, real macro-scale environments such as atmospheric winds exhibit time-varying behavior. In this work, airborne particle communication under time-varying advection is modeled as a linear time-varying (LTV) channel, and a closed-form, time-dependent channel impulse response is derived using the method of moving frames. Based on this formulation, the channel is characterized through its power delay profile, leading to the definition of channel dispersion time as a physically meaningful measure of channel memory and a guideline for symbol duration selection. System-level simulations under directed, time-varying wind conditions show that waveform design is critical for performance, enabling multi-symbol modulation using a single particle type when dispersion is sufficiently controlled. The results demonstrate that time-varying diffusion-advection channels can be systematically modeled and engineered using communication-theoretic tools, providing a realistic foundation for particle-based communication in complex flow environments.

Index Terms—Molecular communication, channel impulse response, digital communication, pulse modulation, gas detectors

I. Introduction

PROPAGATION of energy is used to convey information in conventional communication systems. In contrast, unconventional communication paradigms rely on the propagation of mass to transfer information. Despite the fundamentally different physical mechanisms, both paradigms can be analyzed using the same mathematical framework provided by communication theory. Consequently, the concept of using mass as an information-carrying quantity has been primarily investigated within the literature of molecular communication (MC). MC proposes an unconventional communication paradigm in which molecules are used to encode, transmit, and receive information at both the micro-scale and the macro-scale [1]. Until recently, most studies in MC have focused on the micro-scale domain [2]. However, macro-scale molecular communication has started to attract increasing attention, particularly in scenarios where conventional electromagnetic communication is impractical or unreliable [3]. Moreover, odor-based molecular communica-

Fatih Merdan and O.B. Akan are with the Center for neXt-generation Communications (CXC), Department of Electrical and Electronics Engineering, Koç University, Istanbul 34450, Türkiye (e-mail: fmerdan25@ku.edu.tr, akan@ku.edu.tr).

O. B. Akan is also with the Internet of Everything (IoE) Group, Department of Engineering, University of Cambridge, Cambridge CB3 0FA, U.K. (e-mail: oba21@cam.ac.uk).

tion (OMC), a specialized macro-scale MC paradigm in which information carriers are specific odor molecules, has been widely used to model inter- and intra-species communication in natural systems [4]. Although MC is often motivated by biological contexts, the use of mass to transfer information is a more general concept. For this reason, the term particle is used throughout this paper instead of molecule. In the micro-scale, diffusion alone can be sufficient to support information transfer. In contrast, at the macro-scale, diffusion by itself is inadequate, and advective transport must be explicitly considered [5]. The characterization of advection in diffusion-advection channels—particularly under realistic, time-varying flow conditions—remains an open problem in the context of particle-based communication.

The objective of this paper is to develop a mathematical framework for analyzing diffusion-advection channels from a communication-theoretic perspective. To the best of our knowledge, no exact analytical solution exists for diffusion-advection channels with time-dependent advection in the context of MC. In this work, such a solution is derived, and the resulting time-varying channel is statistically characterized. The implications of the model are interpreted using concepts from classical wireless communication theory. A novel channel classification based on channel dispersion time is introduced to distinguish between dispersive and non-dispersive diffusion-advection channels. Finally, an illustrative airborne particle communication system is constructed under directed wind conditions to demonstrate the feasibility and design implications of the proposed framework.

The remainder of this paper is organized as follows. Section II presents the analytical solution to the time-varying diffusion-advection channel. Section III discusses the implications of the analytical model and introduces the channel dispersion characterization. In Section IV, a representative communication system is analyzed under directed wind conditions. Concluding remarks are given in Section V.

II. Time-varying diffusion-advection Channel

In this Section, to find an analytical expression for a time-varying diffusion-advection channel, the advection term is assumed to be constant in all space but varying in time. In addition, the mean and autocorrelation functions for this channel are determined.

A. Time-varying Channel Impulse Response

The behaviour of particles under diffusion and advection is described with a partial differential equation as

$$\frac{\partial c}{\partial t}(\mathbf{x}, t) = D \nabla^2 c(\mathbf{x}, t) - \mathbf{v}(t) \cdot \nabla c(\mathbf{x}, t) + S(\mathbf{x}, t), \quad (1)$$

where $c(\mathbf{x}, t)$ denotes the concentration of the particle at position \mathbf{x} and time t , D is the constant diffusion coefficient, $\mathbf{v}(t)$ is the wind velocity vector, $\nabla c(\mathbf{x}, t)$ and $\nabla^2 c(\mathbf{x}, t)$ represent the spatial gradient and Laplacian of the concentration, respectively, and $S(\mathbf{x}, t)$ denotes the external source term. The position vector \mathbf{x} is defined as $\mathbf{x} = (\mathbf{x}_{\parallel}, x_3) \in \mathbb{R}^2 \times (0, \infty)$. It is assumed that $x_3 = 0$ is a perfectly absorbing boundary i.e., $c(\mathbf{x}_{\parallel}, 0, t) = 0$ and $c(\mathbf{x}, 0) = c_0(\mathbf{x})$ is the initial particle concentration before transmission. Similarly, the wind velocity vector is defined as $\mathbf{v}(t) = (\mathbf{v}_{\parallel}(t), 0)$ so that the x_3 component of the wind is 0. This means that the gradient term in (1) can be rewritten as

$$-\mathbf{v}(t) \cdot \nabla c(\mathbf{x}, t) = -\mathbf{v}_{\parallel}(t) \cdot \nabla_{\mathbf{x}_{\parallel}} c(\mathbf{x}, t). \quad (2)$$

Defining $\mathbf{r}_{\parallel}(t) \triangleq \int_0^t \mathbf{v}_{\parallel}(\xi) d\xi$, the moving frame variables are introduced as $\mathbf{y}_{\parallel} = \mathbf{x}_{\parallel} - \mathbf{r}_{\parallel}(t)$, $y_3 = x_3$ and $\tau = t$. The transformed concentration field is defined using these variables as $u(\mathbf{y}, t) = c(\mathbf{y}_{\parallel} + \mathbf{r}_{\parallel}(t), y_3, t)$. Defining $\mathbf{y} = (\mathbf{y}_{\parallel}, y_3) = (\mathbf{x}_{\parallel} - \mathbf{r}_{\parallel}(t), x_3)$, the chain rules for dimensions x_1 and x_2 can be written as

$$\begin{aligned} \frac{\partial}{\partial t} c(x, t) &= \frac{\partial}{\partial t} u(y(x, t), \tau(t)) \\ &= u_{\tau}(y, \tau) \frac{\partial \tau}{\partial t} + u_y(y, \tau) \frac{\partial y}{\partial \tau}. \end{aligned} \quad (3)$$

Using the Leibniz rule, $\frac{\partial y}{\partial \tau} = -\frac{dr}{d\tau}(\tau) = -v(\tau)$ is obtained. Therefore, (3) becomes

$$\frac{\partial}{\partial t} c(x, t) = u_{\tau}(y, \tau) - v(\tau) u_y(y, \tau). \quad (4)$$

Moreover, since $\frac{\partial y}{\partial x} = 1$ and $\frac{\partial \tau}{\partial x} = 0$, $\frac{\partial}{\partial x} c(x, t) = u_y(y, \tau)$ and $\frac{\partial^2}{\partial x^2} c(x, t) = u_{yy}(y, \tau)$ are obtained. These relations extend componentwise to the vector case, giving

$$\begin{aligned} \frac{\partial}{\partial \tau} c(\mathbf{x}_{\parallel}, \tau) &= \frac{\partial}{\partial \tau} u(\mathbf{y}_{\parallel}, \tau) - \mathbf{v}_{\parallel}(\tau) \cdot \nabla_{\mathbf{y}_{\parallel}} u(\mathbf{y}_{\parallel}, \tau), \\ \nabla_{\mathbf{x}_{\parallel}} c(\mathbf{x}_{\parallel}, \tau) &= \nabla_{\mathbf{y}_{\parallel}} u(\mathbf{y}_{\parallel}, \tau), \\ \nabla_{\mathbf{x}_{\parallel}}^2 c(\mathbf{x}_{\parallel}, \tau) &= \nabla_{\mathbf{y}_{\parallel}}^2 u(\mathbf{y}_{\parallel}, \tau). \end{aligned} \quad (5)$$

For the x_3 dimension one can obtain

$$u(y_3, \tau) = c(x_3, t),$$

$$\begin{aligned} \frac{\partial}{\partial t} c(x, t) &= \frac{\partial u}{\partial \tau} \frac{\partial \tau}{\partial t} + \frac{\partial u}{\partial y} \frac{\partial y}{\partial t} = \frac{\partial u}{\partial \tau}(y, \tau), \\ \frac{\partial}{\partial x} c(x, t) &= \frac{\partial u}{\partial y}(y, \tau), \\ \frac{\partial^2}{\partial x^2} c(x, t) &= \frac{\partial^2 u}{\partial y^2}(y, \tau). \end{aligned} \quad (6)$$

Thus, using t instead of τ for simplicity with $\mathbf{y} =$

$(\mathbf{y}_{\parallel}, y_3) = (\mathbf{x}_{\parallel} - \mathbf{r}_{\parallel}(t), x_3)$ and $\frac{\partial \mathbf{y}}{\partial t} = \left(-\frac{\partial \mathbf{r}_{\parallel}}{\partial t}, 0 \right) = (-\mathbf{v}_{\parallel}(t), 0)$ one can obtain

$$\frac{\partial}{\partial t} c(\mathbf{x}, t) = \frac{\partial}{\partial t} u(\mathbf{y}, t) - \mathbf{v}_{\parallel}(t) \cdot \nabla_{\mathbf{y}_{\parallel}} u(\mathbf{y}, t). \quad (7)$$

Inserting (5),(6) and (7) into (1), one obtains the transformed PDE as

$$\frac{\partial}{\partial t} u(\mathbf{y}, t) = D \nabla_{\mathbf{y}}^2 u(\mathbf{y}, t) + S(\mathbf{y}_{\parallel} + \mathbf{r}_{\parallel}(t), y_3, t), \quad (8)$$

with the initial and boundary conditions $u(\mathbf{y}, 0) = c_0(\mathbf{y})$, $u(\mathbf{y}_{\parallel}, 0, t) = 0$, respectively. This is a heat equation and its free space kernel is found as [6]

$$\Phi(\mathbf{y}, t) = \begin{cases} \frac{1}{(4\pi D t)^{3/2}} \exp\left(-\frac{\|\mathbf{y}\|^2}{4Dt}\right), & \mathbf{y} \in \mathbb{R}^3, t > 0, \\ 0, & t < 0. \end{cases} \quad (9)$$

Using the method of images, the solution for (8) can be written as

$$\begin{aligned} u(\mathbf{y}, t) &= \int_{\mathbb{R}^3} \Phi_D(\mathbf{y}, \mathbf{z}; t) c_0(\mathbf{z}) d\mathbf{z} \\ &+ \int_0^t \int_{\mathbb{R}^3} \Phi_D(\mathbf{y}, \mathbf{z}; t-s) S(\mathbf{z}_{\parallel} + \mathbf{r}_{\parallel}(s), z_3, s) d\mathbf{z} ds, \end{aligned} \quad (10)$$

where

$$\Phi_D(\mathbf{y}, \mathbf{z}; t) \triangleq \Phi((\mathbf{y}_{\parallel} - \mathbf{z}_{\parallel}, y_3 - z_3, t) - \Phi((\mathbf{y}_{\parallel} - \mathbf{z}_{\parallel}, y_3 + z_3, t)). \quad (11)$$

Returning to the original coordinates, the solution can be written as

$$\begin{aligned} c(\mathbf{x}, t) &= \int_{\mathbb{R}^3} \Phi_D((\mathbf{x}_{\parallel} - \mathbf{r}_{\parallel}(t), x_3), \mathbf{z}; t) c_0(\mathbf{z}) d\mathbf{z} \\ &+ \int_0^t \int_{\mathbb{R}^3} \Phi_D((\mathbf{x}_{\parallel} - \mathbf{r}_{\parallel}(t) + \mathbf{r}_{\parallel}(s), x_3), \mathbf{z}; t-s) \\ &\quad \times S(\mathbf{z}_{\parallel} + \mathbf{r}_{\parallel}(s), z_3, s) d\mathbf{z} ds, \end{aligned} \quad (12)$$

where the $\mathbf{r}_{\parallel}(s)$ terms inside Φ_D originate from the motion of the source relative to the moving coordinate system. Assuming a point source at position \mathbf{z}_0 i.e., $S(\mathbf{z}, s) = q(s) \delta(\mathbf{z} - \mathbf{z}_0)$ and zero initial concentration for the particle, i.e., $c_0(\mathbf{z}) = 0$, the result simplifies as

$$c(\mathbf{x}, t) = \int_0^t \Phi_D((\mathbf{x}_{\parallel} - \mathbf{R}_{\parallel}(t) + \mathbf{R}_{\parallel}(s), x_3), \mathbf{z}_0; t-s) q(s) ds. \quad (13)$$

From (13) for a fixed receiver position, the time-varying channel impulse response can be written as shown in (14). From (14), it is evident that the time-dependent nature of the diffusion-advection channel is due to variations in the wind with time. Under the assumption of constant wind, (14) yields the impulse response of the LTI channel. In that case, (13) becomes a convolution of $h(t)$ with the input to the channel $q(t)$. This assumption may be fine for a very controlled environment, but, in general, it is

$$h(\tau, t) = \frac{1}{(4\pi D\tau)^{3/2}} \left[\exp\left(-\frac{\left\| \mathbf{x}_{\parallel} - \mathbf{z}_{0\parallel} - \int_{t-\tau}^t \mathbf{v}_{\parallel}(\xi) d\xi \right\|^2 + (x_3 - z_{03})^2}{4D\tau}\right) - \exp\left(-\frac{\left\| \mathbf{x}_{\parallel} - \mathbf{z}_{0\parallel} - \int_{t-\tau}^t \mathbf{v}_{\parallel}(\xi) d\xi \right\|^2 + (x_3 + z_{03})^2}{4D\tau}\right) \right]. \quad (14)$$

not possible to control the wind flow with high accuracy.

The Navier-Stokes equations govern the motion of viscous fluid substances. Theoretically, the flow velocity of air, i.e., wind, can be deterministically found. However, since these equations create a chaotic system, the wind is generally taken as a random process for modelling purposes. In this paper, the same convention is followed. In general, Weibull distribution is used to model the wind; although, it is reported that this distribution is not fully comprehensive and one should use other appropriate distributions for each wind regime [7]. Since the objective of this paper is to understand the effect of varying wind on the communication protocols, the wind is assumed to be wide sense stationary (WSS) white Gaussian.

B. Statistical characterization of the time-varying Impulse Response

The derivation of the mean and autocorrelation of (14) requires a preliminary examination of the exponential components of the impulse response, as they contain the stochastic contributions of the wind. Upon expanding the norms, one obtains

$$\begin{aligned} & \left(x_1 - z_{01} - \int_{t-\tau}^t v_1(\lambda) d\lambda \right)^2 + \left(x_2 - z_{02} - \int_{t-\tau}^t v_2(\lambda) d\lambda \right)^2 \\ & + (x_3 - z_{03})^2, \end{aligned} \quad (15)$$

where $v_1(\lambda)$ and $v_2(\lambda)$ are iid jointly Gaussian random processes with mean μ and variance σ_v^2 . $V_1(t) \stackrel{\Delta}{=} \int_{t-\tau}^t v_1(\lambda) d\lambda$ is also a Gaussian process. The mean and variance of V_1 are found as $\mathbb{E}[V_1] = \mu\tau$ and $\text{Var}(V_1) = \sigma_X^2(\tau, t)$, respectively, where

$$\sigma_X^2(\tau, t) \stackrel{\Delta}{=} \int_{t-\tau}^t \int_{t-\tau}^t \text{Cov}(v_1(\lambda_1), v_1(\lambda_2)) d\lambda_1 d\lambda_2, \quad (16)$$

and $\text{Cov}(v_1(\lambda_1), v_1(\lambda_2))$ is the covariance function of v_1 . To represent the random parts in (15), $X_i(t, \tau) \stackrel{\Delta}{=} x_i - z_{0i} - V_i$ are defined for $i = 1, 2$. It is trivial to see that $X_1 \sim \mathcal{N}(x_1 - z_{01} - \mu\tau, (\sigma_X)^2)$ and $X_2 \sim \mathcal{N}(x_2 - z_{02} - \mu\tau, (\sigma_X)^2)$. Since v_1 and v_2 are independent, X_1 and X_2 are also independent. The autocorrelations of X_1 and X_2 are found as $R_{X_1}(\tau_1, \tau_2; t_1, t_2) = (x_1 - z_{01} - \mu\tau_1)(x_1 - z_{01} - \mu\tau_2) + L(\tau_1, \tau_2; t_1, t_2)$ and $R_{X_2}(\tau_1, \tau_2; t_1, t_2) = (x_2 - z_{02} - \mu\tau_1)(x_2 - z_{02} - \mu\tau_2) + L(\tau_1, \tau_2; t_1, t_2)$ respectively, where

$$L(\tau_1, \tau_2; t_1, t_2) \stackrel{\Delta}{=} \int_{t_1-\tau_1}^{t_1} \int_{t_2-\tau_2}^{t_2} \text{Cov}(v_1(\lambda_1), v_1(\lambda_2)) d\lambda_1 d\lambda_2. \quad (17)$$

The time-varying impulse response in (14) can be written as $h(\tau, t) = \beta(\tau) \exp(-\alpha(\tau) [X_1^2(\tau, t) + X_2^2(\tau, t)])$, where

$$\beta(\tau) = \frac{1}{(4\pi D\tau)^{3/2}} \left(e^{-\frac{(x_3 - z_{03})^2}{4D\tau}} - e^{-\frac{(x_3 + z_{03})^2}{4D\tau}} \right), \quad (18)$$

$$\alpha(\tau) = \frac{1}{4D\tau},$$

and the mean and autocorrelation $R_h(\tau_1, \tau_2; t_1, t_2)$ of $h(\tau, t)$ can be expressed as shown in (19) and (20), respectively. For $\mathbf{X} \sim \mathcal{N}_p(\boldsymbol{\mu}, \boldsymbol{\Sigma})$ with $\boldsymbol{\Sigma} > 0$, and $\mathbf{Q} = \mathbf{X}^T \mathbf{A} \mathbf{X}$ where $\mathbf{A} = \mathbf{A}^T$, the moment generating function of \mathbf{Q} is given as [8]

$$\begin{aligned} M_{\mathbf{Q}}(t) &= \mathbb{E}[e^{t\mathbf{Q}}] = |\mathbf{I} - 2t\mathbf{R}|^{-1/2} \\ &\times \exp\left(t\boldsymbol{\mu}^T \boldsymbol{\Sigma}^{-1/2} \mathbf{R} (\mathbf{I} - 2t\mathbf{R})^{-1} \boldsymbol{\Sigma}^{-1/2} \boldsymbol{\mu}\right), \end{aligned} \quad (21)$$

where $\mathbf{R} = (\boldsymbol{\Sigma}^{1/2} \mathbf{A} \boldsymbol{\Sigma}^{1/2})$. Using $p = 2$, inserting $t = \frac{-1}{4D}$ and the following

$$\begin{aligned} \mathbf{X} &= \begin{bmatrix} X_1 \\ X_2 \end{bmatrix} & \mathbf{A} &= \begin{bmatrix} \frac{1}{\tau_1} & 0 \\ 0 & \frac{1}{\tau_2} \end{bmatrix}, \\ \boldsymbol{\mu} &= \begin{bmatrix} x_1 - z_{01} - \mu\tau_1 \\ x_2 - z_{02} - \mu\tau_2 \end{bmatrix}, \end{aligned} \quad (22)$$

$$\boldsymbol{\Sigma} = \begin{bmatrix} \sigma_X^2(\tau_1, t_1) & L(\tau_1, \tau_2; t_1, t_2) \\ L(\tau_1, \tau_2; t_1, t_2) & \sigma_X^2(\tau_2, t_2) \end{bmatrix},$$

to (21) one can obtain an expression for $R_h(\tau_1, \tau_2; t_1, t_2)$. However, when $\tau_1 = \tau_2$ and $t_1 = t_2$, $\boldsymbol{\Sigma}$ becomes singular. The moment generating function of $\mathbf{Q} = \mathbf{X}^T \mathbf{A} \mathbf{X}$, where $\mathbf{A} = \mathbf{A}^T$, and where the $p \times 1$ vector \mathbf{X} is normal with $\mathbb{E}[\mathbf{X}] = \boldsymbol{\mu}$ and $\text{Cov}(\mathbf{X}) = \boldsymbol{\Sigma} = \mathbf{B} \mathbf{B}^T$, with \mathbf{B} being a $p \times r$ matrix of rank $r < p$, is given by [8]

$$\ln M_{\mathbf{Q}}(t) = -\frac{1}{2} \sum_{j=1}^r \ln(1 - 2t\lambda_j) + \alpha t + 2t^2 \sum_{j=1}^r \frac{b_j^2}{1 - 2t\lambda_j}, \quad (23)$$

where $\lambda_1, \dots, \lambda_r$ are the eigenvalues of $\mathbf{B}^T \mathbf{A} \mathbf{B}$, with $\mathbf{B}^T \mathbf{A} \mathbf{B} \neq \mathbf{0}$, $\alpha = \boldsymbol{\mu}^T \mathbf{A} \boldsymbol{\mu}$, $\mathbf{b}^T = \mathbf{P}^T \mathbf{B}^T \mathbf{A} \boldsymbol{\mu}$ and $\mathbf{P} \mathbf{P}^T = \mathbf{I}$. Using $p = 2$, $r = 1$, the same \mathbf{A} and $\boldsymbol{\mu}$ with $\tau_1 = \tau_2$ from (22), inserting $t = \frac{-1}{4D}$ and $\mathbf{B} = [\sigma_X \ \sigma_X]^T$ to (23), one can obtain the expression for $R_h(\tau_1, \tau_2; t_1, t_2)$ for the case where $\tau_1 = \tau_2$ and $t_1 = t_2$. A complete analytical expression for $R_h(\tau_1, \tau_2; t_1, t_2)$ can be obtained with these

$$\mathbb{E}[h(\tau, t)] = \frac{\beta(\tau)}{1 + 2\alpha(\tau) (\sigma_X(\tau, t))^2} \exp\left(-\frac{\alpha(\tau) \left[(x_1 - z_{01} - \mu\tau)^2 + (x_2 - z_{02} - \mu\tau)^2\right]}{1 + 2\alpha(\tau) (\sigma_X(\tau, t))^2}\right). \quad (19)$$

$$R_h(\tau_1, \tau_2; t_1, t_2) = \beta(\tau_1) \beta(\tau_2) \mathbb{E}\left[e^{-\alpha(\tau_1)X_1^2(\tau_1, t_1) - \alpha(\tau_2)X_1^2(\tau_2, t_2)}\right] \mathbb{E}\left[e^{-\alpha(\tau_1)X_2^2(\tau_1, t_1) - \alpha(\tau_2)X_2^2(\tau_2, t_2)}\right]. \quad (20)$$

two cases handled separately.

III. Statistical Analysis and Channel Dispersion Characterization

In this section, observations that follow immediately from the time-varying impulse response definition are discussed, and the similarities between the wireless channels are studied. In addition, using statistical characterizations, the time-varying diffusion-advection channel is classified as non-dispersive and dispersive, and the channel dispersion time, T_d is defined.

A. Effect the of Wind Covariance on the Channel Autocorrelation

The only time dependent components in the autocorrelation of $h(\tau, t)$ are $\sigma_X^2(\tau, t)$ and $L(\tau_1, \tau_2; t_1, t_2)$. Using (16) and (17), it can be shown that when the wind is WSS, the channel also becomes WSS, so it can be represented as $R_h(\tau_1, \tau_2; \Delta t)$. For different definitions of wind covariance, the resulting channel autocorrelation is plotted for $\tau_1 = \tau_2 = 4\text{ s}$. In this analysis, the point source is located at $\mathbf{z}_0 = [0\ 0\ 1]$ and the detection point is located at $\mathbf{x} = [\frac{\sqrt{2}}{2} \frac{\sqrt{2}}{2} 1]$ so that the mean wind flows from the source to the detection point. In addition, the diffusion coefficient of (Z)-3-hexenyl acetate $D = 6.7698 \times 10^{-6} \text{ m}^2/\text{s}$ is used, which is a typical value for particles that travel through the air. Four different wind covariances are used, which are WSS Exponential wind covariance $C_v(t_1, t_2) = (0.2)^2 \exp\left(-\frac{|t_1 - t_2|}{10}\right)$, WSS Gaussian wind covariance $C_v(t_1, t_2) = (0.2)^2 \exp\left(-\left(\frac{t_1 - t_2}{10}\right)^2\right)$, non-stationary Exponential wind covariance $C_v(t_1, t_2) = (0.2)^2 \exp\left(-\frac{|t_1 - t_2|}{10}\right) \exp\left(-\frac{(t_1 + t_2 - 5)^2}{2(30)^2}\right)$ and non-stationary oscillatory wind covariance $C_v(t_1, t_2) = (0.2)^2 \cos\left(\frac{2\pi(t_1 - t_2)}{8}\right) \exp\left(-\frac{|t_1 - t_2|}{10}\right) [1 + 0.3 \sin\left(\frac{t_1 + t_2}{20}\right)]$. The resulting plots are shown in Fig. 1. It can be observed that the channel acts as a decorrelator after a small time difference for a constant delay. Using the Gaussian WSS covariance for the wind with a mean of 0.5 m/s and a standard deviation of 0.2 m/s shown in Fig. 1-(e), the logarithm of $|R_h(\tau_1, \tau_2; t_1, t_2)|$ is plotted against τ_2 for different values of τ_1 and time separation. The resulting plot is given in Fig. 2. It can be observed that as the time separation increases, the autocorrelation between different delays drops drastically. Moreover, from Fig. 2-(a) it can be observed that for a time separation small enough, the autocorrelation again decreases for a delay separation around 5 seconds.

B. Comparison of diffusion-advection and Conventional Time-varying Channels

The similarity between the classical wireless channel and the diffusion-advection channel can be first observed from (13). For both of the channels, a time-varying impulse response is defined. In general, the wireless channels are studied under the wide-sense stationary uncorrelated scattering (WSSUS) assumption. However, the assumption of uncorrelated scattering is not suitable for diffusion-advection channels. This is because particles in the air collide with each other and diffuse together. In a sense, the scatterers in this problem are the information carriers at the same time. In this paper, the comparison between wireless and diffusion-advection channels is conducted using the Power Delay Profile (PDP) of these channels.

The Power Delay Profile $R_h(\tau)$ of the diffusion-advection channel is obtained by inserting $\Delta t = 0$ and $\tau_1 = \tau_2 = \tau$ into the WSS channel autocorrelation function $R_h(\tau_1, \tau_2; \Delta t)$. Four representative wind conditions are examined: (i) dominant wind mean, (ii) comparable wind mean and variance, (iii) dominant wind variance, and (iv) zero wind mean. For each case, PDP is computed at three source-detector separations (1 m , 5 m , 10 m) assuming that the mean wind is directed from the source to the detector. In addition, the Fourier transform of PDP is evaluated only for the 1 meter separation to illustrate how the channel dispersion manifests in the frequency domain. These results are presented in Fig. 3. When the wind mean dominates, a very narrow peak is observed in PDP in the time domain. Increasing the distance only shifts when this peak occurs. As the wind variance increases compared to the wind mean, the time interval in which PDP has a considerable value increases, resulting in a narrower bandwidth in the frequency domain. This means that the channel loses its ability to decorrelate the released particles. When the wind mean is not directed from source to detector, or when the wind mean is zero, establishing a communication system where bit-by-bit transmission is employed is thus not reliable. There is no guarantee that the particles will ever reach the receiver, and even if some particles are detected in the receiver, currently, there is no algorithm that can enable it to decide which particles were released first. This is because the particles in the air remain correlated for a very long time. With the mean wind directed from the source to the detector, a bit-wise communication link can be established. In this topology, the transmitter sends symbols using pulses of a pre-determined duration, and the receiver reads these pulses after they pass through

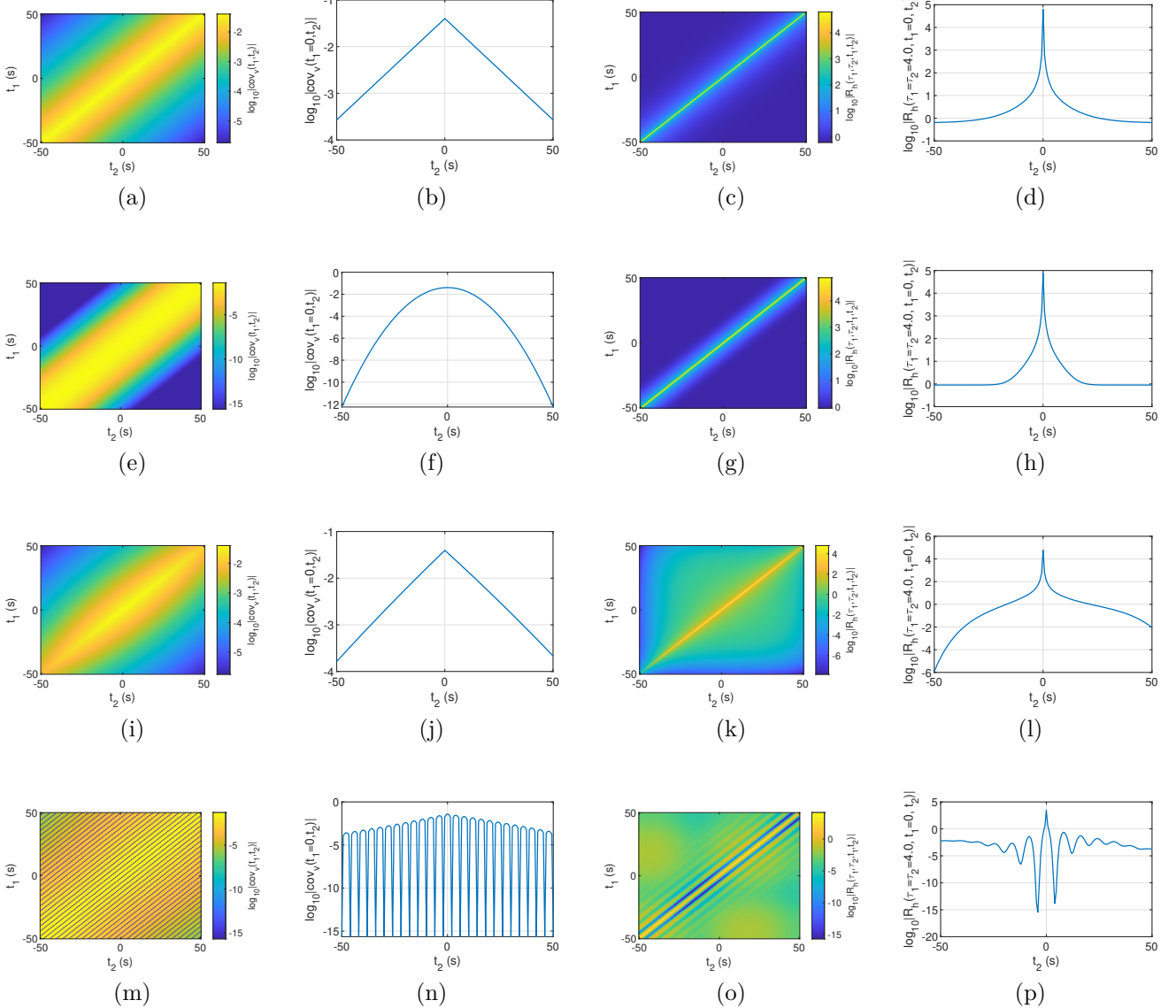


Fig. 1: $R_h(\tau_1 = \tau_2 = 4; t_1, t_2)$ plots for different wind setups: (a) WSS Exponential wind covariance and (b) its slice at $t_1 = 0$, (c) corresponding channel autocorrelation and (d) its slice at $t_1 = 0$; (e) WSS Gaussian wind covariance and (f) its slice at $t_1 = 0$, (g) corresponding channel autocorrelation and (h) its slice at $t_1 = 0$; (i) non-stationary Exponential wind covariance and (j) its slice at $t_1 = 0$ (k) corresponding channel autocorrelation and (l) its slice at $t_1 = 0$; (m) non-stationary oscillatory wind covariance and (n) its slice at $t_1 = 0$ (o) corresponding channel autocorrelation and (p) its slice at $t_1 = 0$.

the channel. This is fully parallel to what happens in a wireless channel. For wireless channels, the initial time where PDP becomes non-zero is of great importance in characterizing the average delay spread of the channel, which is a fundamental design parameter in wireless communication systems. However, when establishing a communication link through a diffusion-advection channel, this definition is not the main design criterion. The first arrival time is mainly determined by the mean wind and the separation between the source and the detector. For a strong directed wind, the initial arrival time does not affect the detection in any other way. This paper proposes

that the main design criterion for a communication link through a diffusion-advection channel is the time length at which PDP remains non-zero. This time length is defined as the channel dispersion time T_d , which is explained in the next section.

C. Channel Dispersion Time

The channel dispersion time shows for that receiver and for that observation time how much different delayed signals are affecting the decision, i.e., it characterizes how different pulses affect each other. To properly define the

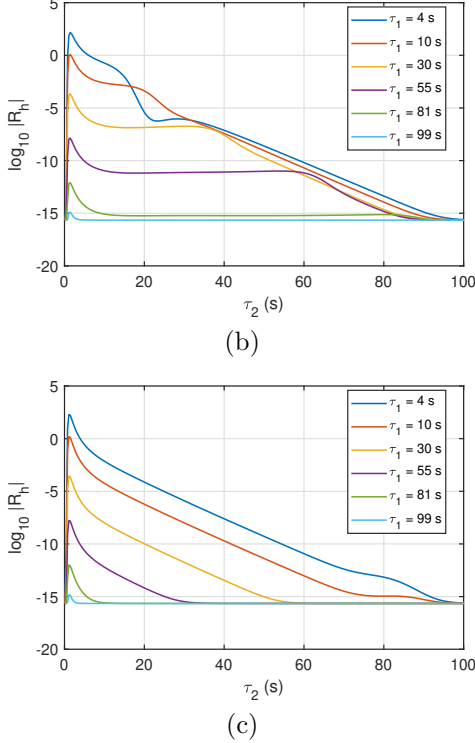
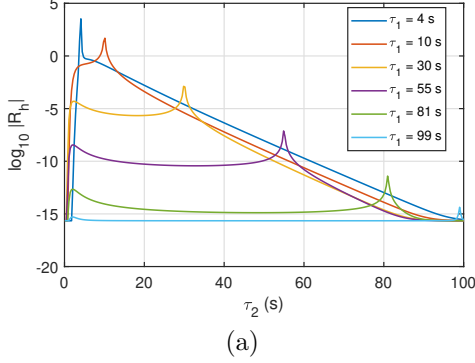


Fig. 2: Logarithm of $R_h(\tau_1, \tau_2; t_1, t_2)$ vs τ_2 for different τ_1 values where $t_1 = 120$ (a) $t_2 = 120$, (b) $t_2 = 130$, and (c) $t_2 = 200$.

channel dispersion time, the PDP of the channel must be considered, which can be written as

$$R_h(\tau) = \beta^2(\tau) \frac{D}{D + \sigma_v^2} \exp\left(-\frac{(x_1 - z_{01} - \mu\tau)^2 + (x_2 - z_{02} - \mu\tau)^2}{2\tau(D + \sigma_v^2)}\right), \quad (24)$$

where the term $(D + \sigma_v^2)$ can be considered as an effective diffusion coefficient, so when the wind variance increases, the diffusion constant the particles feel will be larger. Determination of T_d is related to the Péclet number (P_e), which is a physical constant that characterizes whether advection or diffusion dominates in a flow [9]. Péclet number (P_e) can be written as

$$P_e = \frac{\text{advection rate}}{\text{diffusion rate}} = \frac{L\mu}{D + \sigma_v^2}, \quad (25)$$

where $L = \sqrt{(x_1 - z_{01})^2 + (x_2 - z_{02})^2}$ is the distance between the transmitter and receiver, assuming that both

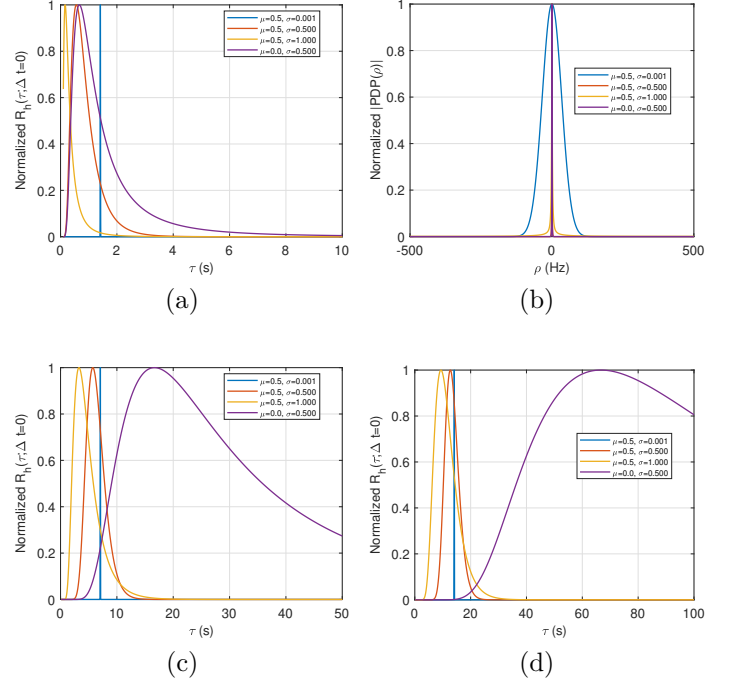


Fig. 3: Power Delay Profile $R_h(\tau)$ of the channel for different wind assumptions at distances of (a) 1 meters, (c) 5 meters, (d) 10 meters and (b) the Fourier transforms of $R_h(\tau)$ for (a).

are in the same height level. If $P_e \gg 10$, advection dominates (wind mean dominates) and using a Gaussian form on (24), one can find T_d as

$$T_d = \sqrt{\frac{[(x_1 - z_{01})^2 + (x_2 - z_{02})^2](D + \sigma_v^2)}{2\sqrt{2}\mu^3}}. \quad (26)$$

T_d is a time-scale that characterizes how long the channel impulse response remains significantly spread in delay due to the combined effects of diffusion and stochastic advection. It depends on the separation between the transmitter and the receiver because increasing the distance increases the particle transit time, during which diffusion and random wind fluctuations accumulate. Using (26) and a symbol duration of T_{sym} , the diffusion-advection channel can be classified as

$$T_{\text{sym}} \geq T_d : \text{Non-dispersive channel}, \\ T_{\text{sym}} < T_d : \text{Dispersive channel}.$$

For symbol durations exceeding the channel dispersion time, the dominant portion of the channel impulse response is confined within a single symbol interval, resulting in reduced inter-symbol interference. In contrast, when the symbol duration is shorter than the dispersion time, significant portions of the impulse response extend beyond one symbol period, leading to persistent ISI. The channel dispersion time T_d is introduced as a design-relevant time scale that quantifies the effective memory of the diffusion-advection channel. It provides a guideline for

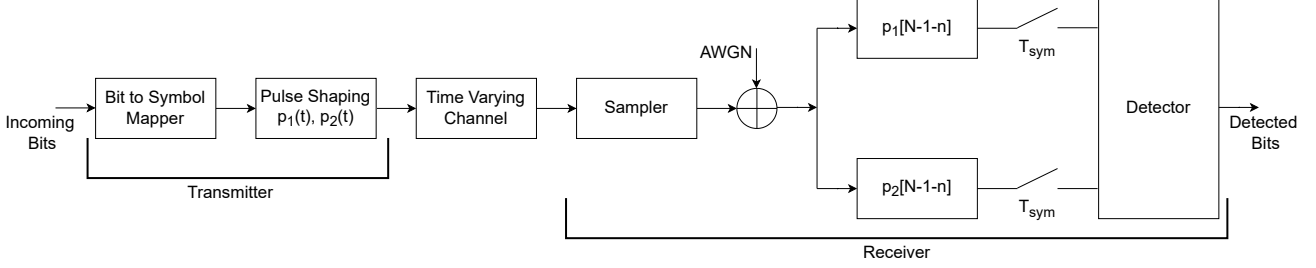


Fig. 4: Block diagram of the complete communication link, including transmitter processing, pulse-shaped emission through the time-varying diffusion-advection channel, sampling with AWGN, and the receiver detection stage.

selecting symbol durations such that the majority of the channel-induced temporal spreading is contained within a single symbol interval. It follows from (26) that increasing the wind variance σ_v^2 increases the channel dispersion time, thereby extending the effective channel memory and necessitating longer symbol durations to limit ISI. Conversely, increasing the mean wind speed μ reduces the dispersion time by accelerating coherent transport, which confines the impulse response in time and enables higher symbol rates. This distinction reveals that reliable airborne particle communication requires directed advection, where transport is dominated by a consistent mean flow component. Under such directed flow conditions, particles experience reduced temporal spreading during propagation. This regime therefore enables predictable arrival structure and bounded channel memory, which are essential for reliable pulse-based communication. In contrast, advection characterized by large variance but weak mean flow lacks directional dominance and leads to increased dispersion.

IV. Communication Under Directed Wind

In this section, a communication topology through a diffusion-advection channel is introduced and analyzed. The block diagram of the proposed system is shown in Fig. 4. The simulations in this section were performed in MATLAB R2023b.

A. Particle Transmitter

The release of particles into the air is a simple procedure. Basically, any type of spray can be considered a possible transmission device. In digital communications, after the information bits are mapped to the designated symbols, application-engineered pulses are used in transmission. The exact modelling scheme is adapted in this paper. The natural way to model particle transmission in time is by using rectangular pulses. The symbol period and the number of orthogonal pulses being used constitute the parameters of the particle pulse shaping design. System shown in Fig. 4 uses two orthogonal rectangle pulses with a symbol period of $T_{sym} = 2$ seconds. The first pulse $p_1(t)$ is 1 for $t \in [0, 1]$ and 0 for $t \in [1, 2]$. The second pulse $p_2(t)$ is the complement of the first one. Therefore, two orthogonal unit energy pulses are utilized in this configuration.

B. Particle Receiver

Gas detectors operate by converting chemical cues into measurable electronic signals, enabling the detection and quantification of various concentrations of gas particles in the air [10], [11]. A short overview of current gas detectors and their working principles is given in Table I. In the context of molecular communications, most studies use MOS gas sensors, since they are simple and easy to experiment with. However, these sensors have a response time of seconds to minutes, which is too slow [12]. Although there are methods to use these sensors in a faster manner, these methods are specific to the detection of bit 1 or 0 [13]. The fastest gas sensors are optical sensors with a response time of milliseconds [14]. These sensors can also operate at room temperature and are tunable to a specific gas particle [15]. If the subtractive demodulation algorithm is used, the receiver becomes linear [16]. It is assumed that the receiver takes many samples from the air in one symbol duration and match filtering is applied in digital domain. The sampling rate of the receiver is taken as 0.1 kHz assuming a linear optical gas sensor is utilized. Moreover, for simplicity of the analysis, the receiver is assumed to directly measure the air concentration without any scaling.

C. Simulation Results for Directed Wind

For simulations, both pulses $p_1(t)$ and $p_2(t)$ are created with a sampling rate of 0.1 kHz in the transmitter to match them exactly in the receiver. Before the signals are given to the channel, they are upconverted to 1 kHz , and the channel is also simulated with this frequency. Only 30 seconds of channel memory is utilized to reduce the computational cost, since the directed wind can already clear out the receiver from the previous pulses within this time. Because of the electronic circuitry of the receiver, an additive white Gaussian noise is added to the sampled channel output. The transmitter is located at $\mathbf{z}_0 = [0 \ 0 \ 1]$ and the receiver is located at $\mathbf{x} = [\frac{\sqrt{2}}{2} \ \frac{\sqrt{2}}{2} \ 1]$ so that a positive mean wind indicates a mean flow from the transmitter to the receiver.

In this system, the receiver samples the concentration of the particle to which it is calibrated all the time. To determine when signalling begins and overcome any symbol timing offset, pilot signals are utilized. In the

TABLE I: Summary of Gas Sensor Types and Operating Principles

Sensor Type	Working Principle	Sensor Type	Working Principle
Catalytic Gas Sensor	Catalytic combustion increases the temperature of a platinum element, changing its resistance [17].	Polymer-Based Gas Sensor	Gas-polymer interaction alters electrical/chemical properties of the polymer layer [18].
Optical Gas Sensor	Measures gas-induced variations in light absorption, reflection, or scattering [19].	Carbon Nanotube (CNT) Gas Sensor	Gas exposure causes charge transfer with nanotubes, modifying their electrical conductivity [20].
Electrochemical Gas Sensor	Target gas undergoes redox reaction; resulting current is proportional to concentration [21].	MOS Gas Sensor	Gas adsorption changes the conductivity of metal oxide semiconductor material [22].
Thermal Conductivity Gas Sensor	Measures heat loss from a heated element to surrounding gas; conductivity varies with gas type [23].	Schottky Diode Gas Sensor	Gas interaction forms a dipole layer at the metal-semiconductor interface, altering Schottky barrier height [24].
Infrared Gas Sensor	Detects gas by IR absorption at characteristic molecular vibration wavelengths [25].	MEMS Gas Sensor	Gas adsorption influences MEMS mechanical/electrical properties (resonance, deflection, conductivity) [26].
Acoustic Wave Gas Sensor	Gas particles interact with the sensing layer and change its properties, altering the propagation of an acoustic wave traveling along the sensor structure [27].	Magnetic Gas Sensor	Gas exposure modifies magnetic properties of the sensing material [28].

TABLE II: Constellation Sets of the Modulation Schemes

Scheme	Constellation Points
2-symbol modulation	(1, 0), (0, 1)
4-symbol modulation	(0, 0), (1, 0), (0, 1), (1, 1)
8-symbol symmetric modulation	(0, 0), (1, 0), (2, 0), (0, 1), (1, 1), (2, 1), (0, 2), (1, 2)
8-symbol wide modulation	(0, 0), (1, 0), (2, 0), (3, 0), (0, 1), (1, 1), (2, 1), (3, 1)
8-symbol tall modulation	(0, 0), (1, 0), (0, 1), (1, 1), (0, 2), (1, 2), (0, 3), (1, 3)
16-symbol modulation	(0, 0), (1, 0), (2, 0), (3, 0), (0, 1), (1, 1), (2, 1), (3, 1), (0, 2), (1, 2), (2, 2), (3, 2), (0, 3), (1, 3), (2, 3), (3, 3)

receiver, a two-step approach is used to find the correct symbol timing. An initial index is determined by scanning the total energy of the output of the matched filters in memory. In the first step, the first index that exceeds 0.05 times the total energy of the output of the matched filters is chosen. In the second step, all possible symbol detection times are tested around the first index, and the inner product between the observed matched filter outputs and the expected symbol shape is calculated. The index maximizing this inner product is chosen as the initial sampling time for detection. Then consecutive samplings are performed with period T_{sym} . To mitigate the channel scaling effect, an MMSE equalizer is used in the signal space. The coefficients of the MMSE equalizer are determined using the pilot signals. Moreover, the additive white Gaussian noise is defined at the output of the sampled channel. Detection is performed using the maximum likelihood criterion that boils down to the minimum euclidean distance. The simulation begins with

the first symbol transmission, and an additional 100 empty symbols are appended after the actual data sequence to allow observation of the channel response after the transmission has ended.

Since the signal is represented by the concentrations of particles, only the part where pulses have nonnegative coefficients can be used in the signal space. Using the two defined orthogonal pulses, six different modulation schemes are inspected. These schemes are summarized in Table II. Taking $\mu = 0.5 \text{ m/s}$, $\sigma_v = 0.001 \text{ m/s}$, $SNR = 10 \text{ dB}$ and $T_{sym} = 2 \text{ s}$, 300 symbols were transmitted using 10 pilot symbols for each modulation type, and the resulting constellations are given in Fig. 5. The simulation results indicate that the receiver is capable of decoding the transmitted signals successfully. This is a promising result, since most studies on molecular communication are limited to using only two different symbols per molecule type, due to the restrictive characteristics of diffusive channels. With controlled advection, one can utilize multi-symbol constellations with a single particle type. This demonstrates that the communication space is not inherently binary, but can be structured through pulse shaping and receiver processing. This shifts the design space from molecule-limited modulation to waveform-limited modulation, where symbol design is governed by channel dispersion and receiver resolution. This can change how we engineer particle-based communications for real-life applications and provide new opportunities. For example, higher data rates can be achieved without increasing the chemical complexity of the system.

To compare the performance of these modulations, the $BER-E_b/N_0$ plots are obtained. In this analysis, the AWGN was defined with respect to the transmitter's average symbol and pulse energies. Moreover, for the signal-noise amplitude match, the channel was normalized to unit energy. $\mu = 0.5 \text{ m/s}$, $\sigma_v = 0.001 \text{ m/s}$, and $T_{sym} = 2 \text{ s}$ were set, and 1000 symbols were transmitted using 10

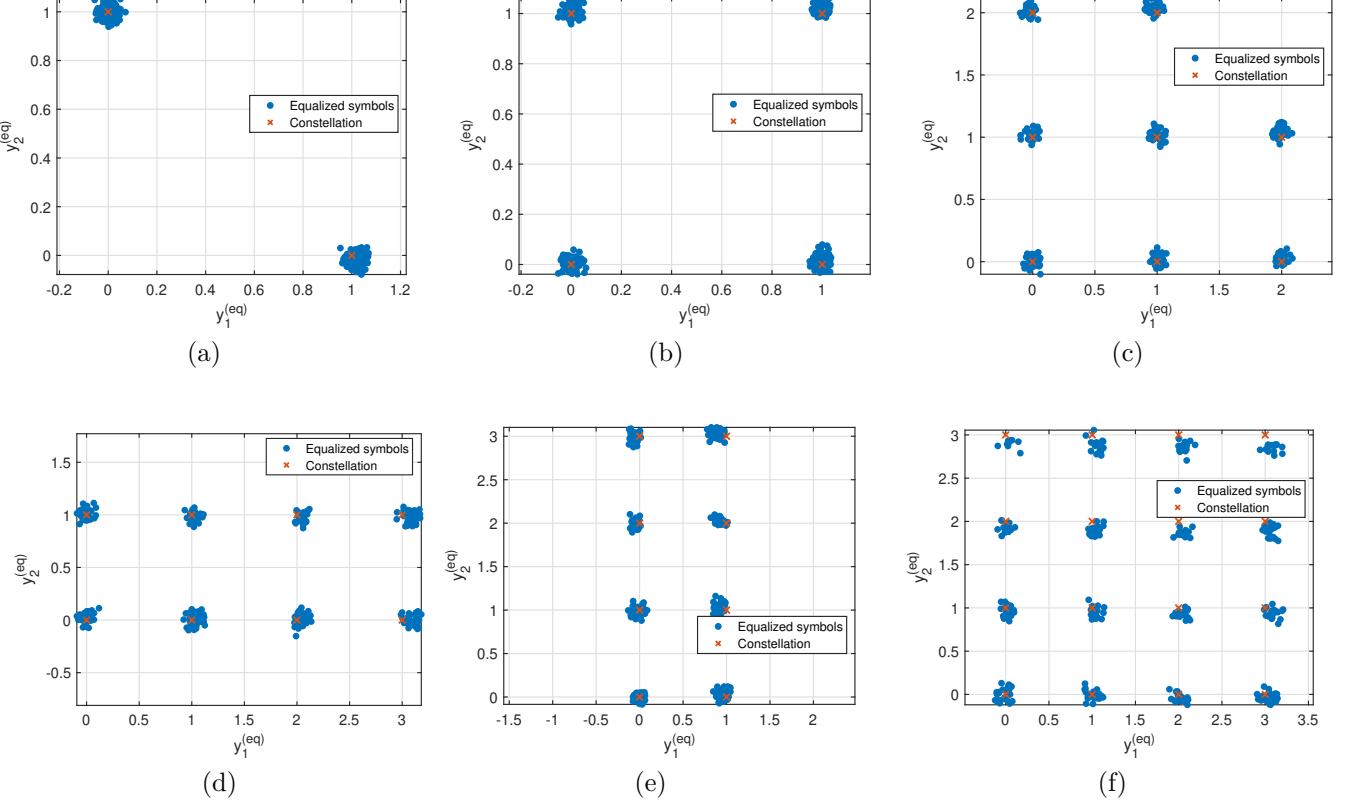


Fig. 5: Constellation diagrams for (a) 2-symbol modulation, (b) 4-symbol modulation, (c) 8-symbol symmetric modulation, (d) 8-symbol wide modulation and (e) 8-symbol tall modulation and (f) 16-symbol modulation.

pilot symbols for each modulation type. Each data point is averaged over 30 independent trials to ensure statistical reliability. The results are shown in Fig. 6. Interestingly, the results show that the optimal modulation is not the lowest-order scheme, but the 4-symbol constellation. This indicates that particle-based channels with controlled advection can benefit from moderate constellation expansion, which improves symbol distinguishability without excessively amplifying noise sensitivity. However, in general, it is observed that as the cardinality of the modulation increases, the performance decreases. It is emphasized that the presented BER results are based on numerical simulations and serve to illustrate the potential benefits and limitations of higher-order modulation in diffusion-advection channels. Confirming these trends under different channel realizations and through experimental studies constitutes an important direction for future work.

To compare dispersive and non-dispersive channels, the 4-symbol modulation scheme is simulated by taking $\mu = 0.07 \text{ m/s}$, $\sigma_v = 0.05 \text{ m/s}$ for different SNR values. In this configuration, the Péclet number is found as 27.92 by (25), and the channel dispersion time is calculated as 1.6 s by (26). In the simulation, 1000 symbols were transmitted using 10 pilot symbols with $T_{sym} = 2 \text{ s}$ corresponding to a non-dispersive channel and $T_{sym} = 1 \text{ s}$ corresponding to a dispersive channel. The resulting BER-SNR plot is given in Fig. 7 and show that a communication

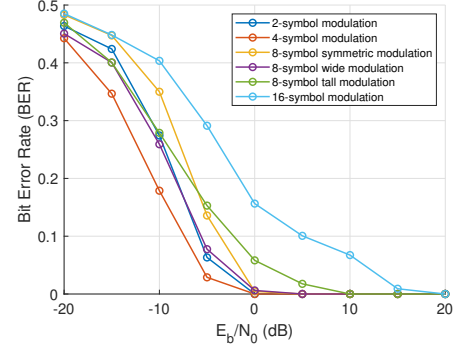


Fig. 6: BER performance of the six modulation schemes as a function of E_b/N_0 .

link over both of the channels seems achievable for high enough SNR. Although a reduction in symbol duration is expected to increase the error rate in general, the results in Fig. 7 reveal that the observed performance degradation cannot be attributed solely to noise. Instead, the degradation persists across the SNR range due to increased inter-symbol interference induced by channel dispersion. The purpose of this comparison is to show that the proposed dispersion time provides a principled criterion for determining when rate reduction becomes necessary due to channel memory rather than noise.

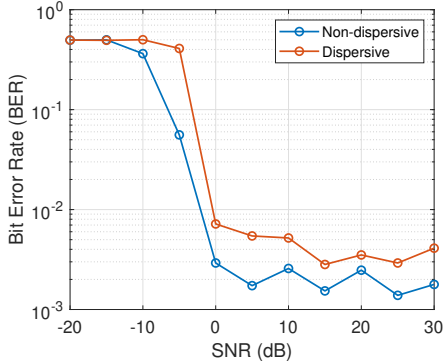


Fig. 7: BER comparison between dispersive and non-dispersive channels across varying SNR levels.

D. Optimum Particle Pulse Shape

In this section, a metric for determining the optimum particle pulse shape is introduced. In the context of this paper, the optimal pulse is the pulse that enables reliable communication as fast as the diffusion-advection channel allows. There are two parameters with which the pulse used can be optimized, which are the symbol period T_{sym} and the signalling dimension N . Since the purpose is to understand the effects of the channel on the pulse shape, the AWGN is ignored in this analysis.

Because the signals are nonnegative under particle communication, the only way to create orthogonal pulses is to separate them in the given symbol period so that only one of them is positive at a time instance. Here, the symbol period is divided into N equal segments, each corresponding to one dimension in the signal space. For this analysis wind mean is taken as $\mu = 0.5 \text{ m/s}$. Wind variance is taken as $\sigma_v = 0.001 \text{ m/s}$ for an advection dominated flow ($P_e = 64351$) and $\sigma_v = 0.4 \text{ m/s}$ for a diffusion dominated flow ($P_e = 3.12$). To have reliable communication, after the pulse is passed through the channel, in the receiver, the matched filters corresponding to the orthogonal pulses must yield the smallest total energy possible. Defining pulses as p_1, p_2, \dots, p_N and using the nonnegativity of the signals, this observation can be formalized as

$$\sum_{i=1}^N \sum_{\substack{j=1 \\ j \neq i}}^N c_i(t) * p_j^{\text{MF}}(t), \quad (27)$$

where $c_i(t)$ is the channel output calculated using (13) for an input pulse $p_i(t)$. The total pulse leakage defined in (27) measures intra-symbol waveform interference induced by the channel, rather than inter-symbol interference caused by symbol sequencing. A pulse set with a smaller total pulse leakage is better in terms of maintaining the separability of the transmitted waveforms after channel propagation, which directly improves the robustness of pulse-based signaling under diffusion-advection dynamics. Unlike BER-based performance metrics, which conflate noise, symbol sequencing, and detection effects, the total pulse leakage provides a structural measure of pulse

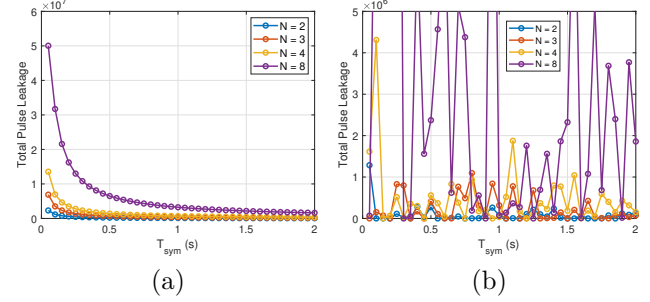


Fig. 8: Total pulse leakage versus symbol duration T_{sym} for different signalling dimensions N for (a) advection dominated flow and (b) diffusion dominated flow.

separability after propagation. As such, it serves as a diagnostic tool for evaluating the suitability of a pulse set before considering specific modulation formats or symbol streams. The value of this sum is plotted against T_{sym} for different N values, where only a single pulse is transmitted to isolate the distortion introduced by the channel and receiver processing for flows dominated by advection and diffusion. The results are given in Fig. 8. In advection-dominated flows, the rapid transport of particles preserves the temporal localization of pulses, resulting in reduced overlap between the channel-distorted responses of different pulses as T_{sym} increases. Consequently, although $N = 2$ yields the lowest leakage for short symbol durations, larger pulse sets become viable at longer T_{sym} , enabling higher-dimensional signaling. In contrast, for diffusion-dominated flows, increasing T_{sym} does not lead to a comparable reduction in total pulse leakage. This indicates that diffusion causes persistent temporal spreading that degrades pulse orthogonality regardless of symbol duration. As a result, the channel-induced mixing of pulses becomes intrinsic, rather than rate-dependent. While the previous analyses primarily focused on advection-dominated regimes where reliable symbol detection is achievable, diffusion-dominated channels represent a fundamentally different operating condition in which severe waveform mixing can prevent meaningful symbol-level decoding. In such cases, BER alone is insufficient to characterize system behavior, and structural metrics such as total pulse leakage provide insight into the feasibility of pulse-based signaling itself.

V. Conclusion

In this paper, a time-varying diffusion-advection channel is analytically characterized using the method of moving frames, yielding a closed-form, time-dependent channel impulse response. Based on this formulation, the channel is analyzed through its mean behavior and temporal correlation structure, enabling a principled characterization of channel memory. Channel dispersion time is defined as a physically meaningful time scale that governs symbol duration selection and achievable communication rates. This leads to a dispersion-based classification of

diffusion–advection channels that directly links channel physics to communication system design. Building on this analytical foundation, an airborne particle communication system is investigated under directed wind conditions. The results demonstrate that, despite the fundamentally different propagation mechanisms, many core concepts from conventional digital communication remain applicable when appropriately adapted to mass-based signaling. Importantly, the analysis reveals that the communication space in airborne particle systems is not inherently binary. Instead, multi-symbol constellations can be realized using a single particle type by exploiting waveform design and receiver processing, shifting the modulation paradigm from molecule-limited to waveform-limited signaling. Total pulse leakage metric is introduced as a structural measure of pulse separability under channel-induced distortion. This metric provides insight into the feasibility of higher-dimensional signaling independent of symbol sequencing and noise, and reveals fundamental differences between advection-dominated and diffusion-dominated regimes. In particular, the results show that diffusion-dominated transport leads to intrinsic waveform mixing that limits reliable communication regardless of symbol duration.

Beyond the airborne communication scenario considered, the proposed framework can be used to engineer any diffusion–advection links. One practical use case is industrial monitoring when RF communication is unreliable, such as in tunnels and underground galleries. In agriculture, the model is directly relevant to volatile organic compound-driven plant signaling experiments and to greenhouse monitoring, where volatile releases and distributed sensors can track stress, disease progression, or treatment response. In the micro-scale, the same dispersion- and memory-based design rules can be applied to microfluidic and lab-on-chip settings. This includes targeted delivery and sensing in microchannels, timing-coded chemical assays, and flow-based biosensing. More broadly, the analysis extends to systems involving charged particle transport under externally applied fields, where particle motion is governed by a combination of diffusion, drift, and field-induced advection. In such settings, time-varying electric or magnetic fields can introduce controlled, directed transport analogous to advection. Across all these domains, dispersion time and pulse leakage provide actionable design rules that determine feasible symbol durations, achievable signaling rates, and the dimensionality of the usable signal space under the prevailing transport dynamics. Future research directions include extending the framework to multi-particle signaling with heterogeneous receivers, adaptive modulation and symbol timing based on real-time dispersion estimates, and experimental validation in controlled wind and flow environments. Additional opportunities arise in joint sensing-and-communication paradigms, where the same particle signals used for communication can simultaneously probe environmental conditions such as flow variability or turbulence. Together, these directions point toward a new class of mass-based communication and sensing systems

that can be systematically analyzed and engineered using the tools developed in this work.

References

- [1] D. Kilinc and O. B. Akan, “Receiver Design for Molecular Communication,” *IEEE Journal on Selected Areas in Communications*, vol. 31, no. 12, pp. 705–714, December 2013.
- [2] O. B. Akan, H. Ramezani, T. Khan, N. A. Abbasi, and M. Kuscu, “Fundamentals of Molecular Information and Communication Science,” *Proceedings of the IEEE*, vol. 105, no. 2, pp. 306–318, February 2017.
- [3] M. M. Al-Zubi and M.-S. Alouini, “Macroscopic Molecular Communication in IoT-Based Pipeline Inspection and Monitoring Applications: Preliminary Experiment and Mathematical Model,” *IEEE Open Journal of the Communications Society*, vol. 6, pp. 7541–7554, 2025.
- [4] A. B. Kilic and O. B. Akan, “End-to-End Mathematical Modeling of Stress Communication Between Plants,” October 2024.
- [5] D. T. McGuiness, S. Giannoukos, A. Marshall, and S. Taylor, “Modulation Analysis in Macro-Molecular Communications,” *IEEE Access*, vol. 7, pp. 11049–11065, 2019.
- [6] L. C. Evans, *Partial Differential Equations*, 2nd ed., ser. *Graduate Studies in Mathematics*. Providence, RI: American Mathematical Society, 2010, vol. 19.
- [7] J. A. Carta, P. Ramírez, and S. Velázquez, “A review of wind speed probability distributions used in wind energy analysis: Case studies in the Canary Islands,” *Renewable and Sustainable Energy Reviews*, vol. 13, no. 5, pp. 933–955, June 2009.
- [8] A. M. Mathai and S. B. Provost, *Quadratic Forms in Random Variables: Theory and Applications*, ser. *Statistics: Textbooks and Monographs*. New York, NY: Marcel Dekker, Inc., 1992, vol. 126.
- [9] W. Wicke, T. Schwering, A. Ahmadzadeh, V. Jamali, A. Noel, and R. Schober, “Modeling Duct Flow for Molecular Communication,” in *2018 IEEE Global Communications Conference (GLOBECOM)*, December 2018, pp. 206–212.
- [10] S. Panda, S. Mehlawat, N. Dhariwal, A. Kumar, and A. Sanger, “Comprehensive review on gas sensors: Unveiling recent developments and addressing challenges,” *Materials Science and Engineering: B*, vol. 308, p. 117616, October 2024.
- [11] Z. Yunusa, M. Hamidon, A. Kaiser, and Z. Awang, “Gas sensors: A review,” 2014.
- [12] J. Burgues, L. F. Valdez, and S. Marco, “High-bandwidth e-nose for rapid tracking of turbulent plumes,” in *2019 IEEE International Symposium on Olfaction and Electronic Nose (ISOEN)*. Fukuoka, Japan: IEEE, May 2019, pp. 1–3.
- [13] D. Drix and M. Schmuker, “Resolving Fast Gas Transients with Metal Oxide Sensors,” *ACS Sensors*, vol. 6, no. 3, pp. 688–692, March 2021.
- [14] S. Thomas, H. H. Chen, and S. W. Pang, “Response Time for Optical Emission and Mass Spectrometric Signals During Etching of Heterostructures,” *MRS Online Proceedings Library*, vol. 406, no. 1, pp. 27–32, December 1995.
- [15] S. Bhattacharjee et al., “Exhaled Breath Analysis Through the Lens of Molecular Communication: A Survey,” *IEEE Communications Surveys & Tutorials*, pp. 1–1, 2025.
- [16] S. Lin, J. Chang, J. Sun, and P. Xu, “Improvement of the Detection Sensitivity for Tunable Diode Laser Absorption Spectroscopy: A Review,” *Frontiers in Physics*, vol. 10, March 2022.
- [17] L. Xu, T. Li, X. Gao, and Y. Wang, “A high heating efficiency two-beam microhotplate for catalytic gas sensors,” *2012 7th IEEE International Conference on Nano/Micro Engineered and Molecular Systems (NEMS)*, pp. 65–68, March 2012.
- [18] A. Verma, R. Gupta, A. S. Verma, and T. Kumar, “A review of composite conducting polymer-based sensors for detection of industrial waste gases,” *Sensors and Actuators Reports*, vol. 5, p. 100143, June 2023.
- [19] J. Hodgkinson and R. P. Tatam, “Optical gas sensing: A review,” *Measurement Science and Technology*, vol. 24, no. 1, p. 012004, November 2012.
- [20] S. Shen et al., “An LC Passive Wireless Gas Sensor Based on PANI/CNT Composite,” *Sensors*, vol. 18, no. 9, p. 3022, September 2018.
- [21] M. Serafini et al., “A Wearable Electrochemical Gas Sensor for Ammonia Detection,” *Sensors*, vol. 21, no. 23, p. 7905, January 2021.

- [22] H.-J. Kim and J.-H. Lee, "Highly sensitive and selective gas sensors using p-type oxide semiconductors: Overview," *Sensors and Actuators B: Chemical*, vol. 192, pp. 607–627, March 2014.
- [23] C. Wang, B. Jiao, X. Liu, C. Zhao, G. Wu, and R. Liu, "Design of Thermal Conductivity Gas Sensor with Silicon Cap," in 2023 IEEE 16th International Conference on Electronic Measurement & Instruments (ICEMI). Harbin, China: IEEE, August 2023, pp. 204–208.
- [24] S. Das, S. Majumdar, R. Kumar, A. Chakraborty, A. Bag, and D. Biswas, "Simplified gas sensor model based on AlGaN/GaN heterostructure Schottky diode," *AIP Conference Proceedings*, vol. 1675, no. 1, p. 020014, August 2015.
- [25] M. Xu et al., "A design of an ultra-compact infrared gas sensor for respiratory quotient (qCO₂) detection," *Sensors and Actuators A: Physical*, vol. 331, p. 112953, November 2021.
- [26] M. Barzegar Gerdroodbary, D. D. Ganji, I. Shiryanpour, and R. Moradi, "Mass analysis of CH₄/SO₂ gas mixture by low-pressure MEMS gas sensor," *Journal of Natural Gas Science and Engineering*, vol. 53, pp. 317–328, May 2018.
- [27] R. Hopper, D. Popa, F. Udrea, S. Z. Ali, and P. Stanley-Marbell, "Miniaturized thermal acoustic gas sensor based on a CMOS microhotplate and MEMS microphone," *Scientific Reports*, vol. 12, no. 1, p. 1690, February 2022.
- [28] P. V. Shinde and C. S. Rout, "Magnetic gas sensing: Working principles and recent developments," *Nanoscale Advances*, vol. 3, no. 6, pp. 1551–1568, March 2021.



Fatih Merdan completed his high school education at Kirikkale Science High School. He received his B.Sc. degree in Electrical and Electronics Engineering from Middle East Technical University. He is currently pursuing his M.Sc. degree in Electrical and Electronics Engineering under the supervision of Prof. Akan at Koç University, Istanbul, Turkey.



Ozgur B. Akan (Fellow, IEEE) received the PhD from the School of Electrical and Computer Engineering Georgia Institute of Technology Atlanta, in 2004. He is currently the Head of Internet of Everything (IoE) Group, with the Department of Engineering, University of Cambridge, UK and the Director of Centre for neXt-generation Communications (CXC), Koç University, Turkey. His research interests include wireless, nano, and molecular communications and Internet of Everything.